CONTROL OF ACTIVE PENDULUM FOR CONTACT DYNAMICS SIMULATION

A Thesis

by

ABHAY HIREN MASHER

Submitted to the Office of Graduate **and Professional** Studies of
Texas A&M University
in partial fulfillment of the requirements for the degree of

MASTER OF SCIENCE

Chair of Committee,	John L. Junkins
Co-Chair of Committee,	John E. Hurtado
Committee Member,	Pilwon Hur
Head of Department,	Rodney D. W. Bowersox

December 2016

Major Subject: Aerospace Engineering

ABSTRACT

Space proximity missions essentially need on the ground hardware in the loop (HIL) testing of sensors, algorithms, and actuators. Such testing would surpass that of software only simulations and would mature hardware and software to vastly reduce risk of close proximity operations. Simulation of interaction dynamics in proximity operations is very difficult. An active pendulum system can be used to simulate these important contact dynamics. The pendulum system can be commanded to track trajectories which represent plausible contact dynamic motions. The pendulum system can also be used to investigate unknown contact dynamics. With an external robot to simulate spacecraft motion, a payload on the gantry system can be subjected to contact forces. The pendulum system actively moves the payload to simulate planar space-like contact dynamics throughout and after the interaction. This thesis develops high fidelity and first principle based controllers to allow for simulation of both prescribed and unknown planar contact dynamics. A linear quadratic integral controller is designed for trajectory tracking. This controller is compared with a nonlinear trajectory tracking controller developed using partial feedback linearization. To simulate unknown contact dynamics a controller is developed using uncollocated partial feedback linearization. The three controllers are analyzed and compared using several test cases in software simulation. The nonlinear trajectory tracking controller is shown to outperform the linear controller. Simulation results also indicate that the unknown contact dynamics controller outperforms the trajectory tracking controllers in the neighborhood surrounding interactions.

ii

To my family, for their love and support

ACKNOWLEDGEMENTS

TABLE OF CONTENTS

Page

LIST OF FIGURES

LIST OF TABLES

CHAPTER I

INTRODUCTION

With the growing space object population, space proximity operations will be increasingly common. There are over 20,000 pieces of orbital debris larger than softball size currently orbiting the earth. Some studies indicate that the current debris population will continue to grow unbounded unless action is taken to reduce the population [2,3]. A NASA study shows that by annually removing a small number of large objects from orbit, we can reduce the debris population so the collision risk due to debris can be greatly reduced [4]. Apart from orbital debris removal, other uncooperative missions include docking for repair of a spacecraft, while cooperative proximity operations could also include satellite refueling or payload transfer.

Proximity missions essentially need on the ground hardware in the loop (HIL) testing of sensors, algorithms, and actuators. Such testing would surpass that of software only simulations and would mature hardware and software to vastly reduce risk of close proximity operations. To help answer this need, several systems have been developed in industry, academia, and government labs. Lockheed Martin has developed a testbed in their Space Operations Simulation Center which allows for HIL proximity operations testing [5]. The Lockheed system allows for full scale simulation using robotic assemblies which provide both vertical and planar actuation. The vehicle dynamics are simulated in software and the hardware is commanded to follow a calculated trajectory. Likewise, the Naval Research Laboratory has a frequently used facility where proximity operations using either research prototypes

or flight hardware can be tested [6]. The Jet Propulsion Lab also has a similar test facility [7].

Analytical modeling of contact dynamics between space objects is very difficult. If the interaction force history is known, a reference trajectory for robot tracking could be generated. Then the interaction could be simulated using existing testbeds. However in cases where the contact forces are unknown, the aforementioned testbeds are no longer suitable.

In [8] Probe designs and builds an active pendulum system which can be used to simulate contact dynamics. Importantly, not only can such a pendulum system can be used to track reference trajectories as in prior testbeds, but can also be used to simulate interactions with unknown contact dynamics. Simulations of unknown contact dynamics do not prescribe interaction behavior but rather create conditions in which interaction behavior can be observed. This eliminates the requirement of complex interaction modeling for the HIL simulation.

Probe's work introduced the use an active pendulum system for contact dynamics testing [8], [9]. NASA Johnson Space Center prior developed a gravity offload system based around a gantry crane [10]. This system is used to provide humans attached to the pendulum a simulation of the space environment. The NASA system relies on the same principles developed in section IV.A. More recently, Hockman developed a similar gravity offload testbed for micro-robot testing [11].

Controller design is made challenging because the system dynamics are both nonlinear and underactuated. The tracking problem for the active pendulum system has long been studied. Kumar [12] develops optimal control to track pendulum

trajectories. Omar develops robust gantry crane controllers in [13]. In [14] Wang develops sliding mode based trajectory tracking controllers. Partial feedback linearization based controllers are developed by several authors [15], [16], [17].

While simulating unknown contact dynamics, a payload on the gantry system can be subjected to contact forces delivered from an external robot (e.g. [18, 19]). By regulating the pendulum angle and angular rate, the dynamics keep the body mass center in a horizontal plane and the in-plane acceleration is very nearly due to only the external force (pendulum dynamics rendered negligible). The control methodology holds valid for both sustained or impulsive contact. Because the body is very nearly suspended by it's mass center, the rotational dynamics have near negligible suspension system torques. The rotational dynamics are dominated by the external torques due to the contact induced torques.

The research in this thesis improves upon Probe's results [8] by developing higher fidelity and improved first principle based controllers to allow for simulation of both prescribed and unknown interaction dynamics. The work is structured as follows. High fidelity planar dynamics are derived using first principles. The system is linearized and a linear quadratic integral trajectory tracking controller is designed. A nonlinear trajectory tracking controller is designed using collocated feedback linearization. A novel application of partial feedback linearization is used to develop a controller to simulate unknown contact dynamics. The controllers are analyzed and compared using software simulation. A brief discussion of hardware difficulties is presented.

SYSTEM DYNAMICS

In this chapter a high fidelity system model is created. The dynamics for the cart pole system are found. The actuator dynamics are derived using a motor model. The motor dynamics are inserted into the cart pole dynamics to construct a full system model.

II.A. Cart Pole System

The dynamics for the cart pole system are found using the Lagrangian approach. As shown in Figure II.1 the system is modeled as a generalized pendulum [20] hanging from a cart. In the diagram, the variables are defined as follows: m_c is cart mass, m_p is pendulum mass, F_m is motor force on cart, J_{pend} is moment of inertia of pendulum, x is horizontal position state, θ is angle state, F_d is disturbance force caused through contact.

The position vectors for the cart and pendulum are shown in equations 2.1 and 2.2. L_{com} is the distance from the cart to the center of mass of the pendulum. The kinetic energy of each body can be seen in equations 2.3 and 2.4. Equation 2.5 shows the Lagrangian which is formulated using the potential energy and kinetic energy.

$$p_{cart} = \begin{bmatrix} x & 0 \end{bmatrix}^T \tag{2.1}$$
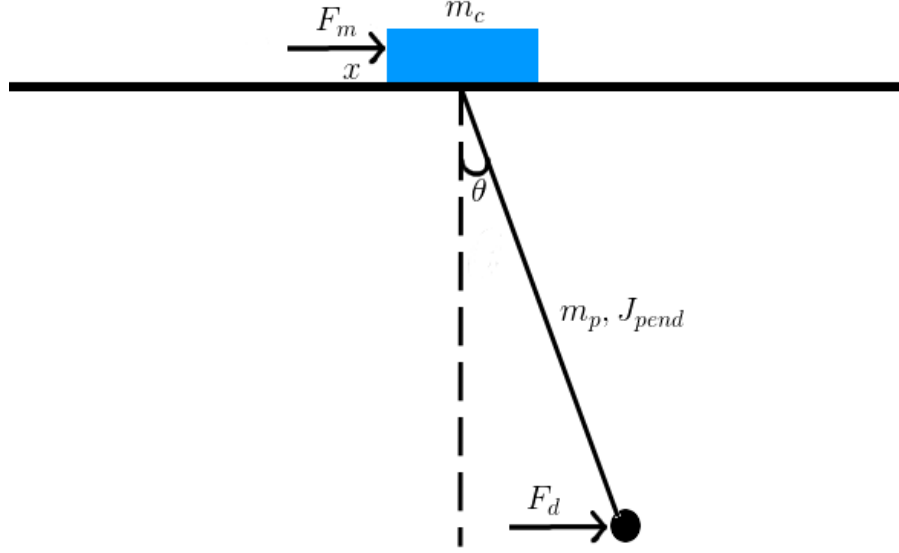
Figure II.1. System model

$$p_{pend} = \left[(x + L_{com} \sin \theta) \quad (-L_{com} \cos \theta) \right]^T \tag{2.2}$$

$$T_{cart} = \frac{1}{2} m_c \dot{x}^2 \tag{2.3}$$

$$T_{pend} = \frac{1}{2} m_p [\dot{x}^2 + L_{com}^2 \dot{\theta}^2 + 2\dot{x} L_{com} \dot{\theta} \cos \theta] + \frac{1}{2} J_{pend} \dot{\theta}^2 \tag{2.4}$$

$$\begin{aligned} L &= T - V \\ &= \frac{1}{2} \dot{x}^2 (m_c + m_p) + \frac{1}{2} \dot{\theta}^2 (m_p L_{com}^2 + J_{pend}) + m_p L_{com} \cos \theta \dot{x} \dot{\theta} + m_p g L_{com} \cos \theta \end{aligned} \tag{2.5}$$

The cart is acted on by the motor force only and experiences no torques. The pendulum is torqued by the external contact disturbance F_d and is also acted on by a damping torque. The generalized forces are shown in equations 2.6 and 2.7. The

5

damping coefficient is given by d_p, and L_{pend} is the total length of the pendulum. Using Lagrange's relation shown in equation 2.8, we find the cart-pole dynamics shown in equations 2.9 and 2.10.

$$Q_{\dot{\theta}} = -d_p\dot{\theta} + F_d(L_{pend} - L_{com}) \tag{2.6}$$

$$Q_{\dot{x}} = F_m \tag{2.7}$$

$$\frac{d}{dt}\frac{\partial L}{\partial \dot{q}_i} - \frac{\partial L}{\partial q_i} = Q_{\dot{q}_i}, q = [\theta, x] \tag{2.8}$$

$$(m_c + m_p)\frac{d^2x}{dt^2} + L_{com}\cos(\theta)m_p\frac{d^2\theta}{dt^2} + L_{com}(-\sin(\theta))m_p\left(\frac{d\theta}{dt}\right)^2 = F_m \tag{2.9}$$

$$\begin{aligned}\frac{d^2\theta}{dt^2}\left(J_{pend} + L_{com}^2 m_p\right) + gL_{com}\sin(\theta)m_p + L_{com}\cos(\theta)m_p\frac{d^2x}{dt^2} \\ = F_d\cos(\theta)\left(L_{pend} - L_{com}\right) - d_p\frac{d\theta}{dt}\end{aligned} \tag{2.10}$$

II.B. Motor Model

The motor model is derived using the procedure described by Ogata in [21]. As shown in Figure II.2 the standard model consists of an RL circuit. The variables are defined as follows: L is the motor inductance, R_a is the internal motor resistance, V_a is the applied voltage, V_m is the voltage across the motor, J_m is the motor inertia. The differential equation is shown in equation 2.11.

$$L\frac{di_a}{dt} + R_a i_a + V_m = V_a \tag{2.11}$$
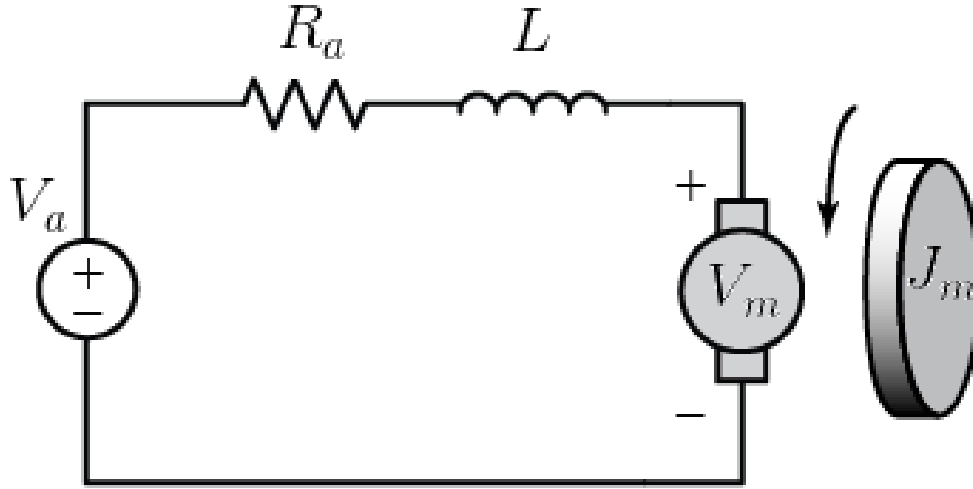
Figure II.2. Motor model [1]

The input voltage V_a can be written as a control signal e_v multiplied by a gain K_1. Using this relation and the motor back emf constant K_3, we rewrite equation 2.11 as shown in equation 2.12. Applying a laplace transform and using the motor torque constant K_2 to relate current to torque, we find the total torque as shown in equation 2.13. By regarding the inductance as small and negligible the motor model can be reduced from third order to second order (see equation 2.14).

$$L\frac{di_a}{dt} + R_a i_a + K_3\frac{d\phi}{dt} = K_1 e_v \tag{2.12}$$

$$T_{net}(s) = \frac{K_2 K_1 e_v - K_2 K_3 \phi(s)}{L_a s + R_a} \tag{2.13}$$

$$T_{net}(s) = \frac{K_2 K_1 e_v - K_2 K_3 \phi(s)}{R_a} \tag{2.14}$$

The net torque is the sum of the torques required to drive the pendulum, all actuator components (belt, pulleys), and motor itself [22, 23]. This is shown in equation 2.15. We rewrite the torque expression to include any gearbox, and convert the motor rotation variable to the linear position of the cart, the result of which is shown in equation 2.16. Constants are as follows: N_2 is an actuator parameter for converting rotations to linear translation (radians to meters), d_b damping constant on belt, m_{belt} mass of belt, R_p radius of pulley in actuator, J_{pulley} pulley inertia, N_1 gearbox ratio (external/internal).

$$T_{net} = T_{pendsys} + T_{pulleys} + T_{belt} + T_{friction} + T_{motor} \tag{2.15}$$

$$T_{net} = \frac{1}{N_1}[RF_m + N_2 \ddot{x}(2 J_{pulley} + m_{\text{belt}} R^2 + J_{motor}) + d_b \dot{x} N_2] \tag{2.16}$$

Substituting the final torque expression in equation 2.14 into equation 2.16 we solve for the force on the pendulum system. Equation 2.17 describes the force on the pendulum system for a given motor input based on actuator and motor characteristics.

$$\begin{aligned} N_2 R_a d_b \frac{dx}{dt} + N_2 R_a m_{\text{belt}} R_p^2 \frac{d^2 x}{dt^2} + N_2 R_a J_{\text{motor}} \frac{d^2 x}{dt^2} \\ + 2 N_2 R_a J_{\text{pulley}} \frac{d^2 x}{dt^2} - k_1 k_2 N_1 e_v + k_2 k_3 N_2 N_1^2 \frac{dx}{dt} = -(R_a R_p) F_m \end{aligned} \tag{2.17}$$

II.C.   Combined System Model

Inserting equation 2.17 into equation 2.9 we can eliminate F_m. Together with equation 2.10 we have a full system description. The combined dynamics can be written in standard form [24] as shown in equations 2.19, 2.18. The h_1, h_2 expressions are functions of the generalized coordinates and their derivatives, while the ϕ expression is a function of the coordinates only. This form separates the actuated state from the unactuated state. The various coefficients are defined in equations 2.20 through 2.27.

$$d_{11}\frac{d^2\theta}{dt^2} + d_{12}\frac{d^2 x}{dt^2} + h_1 + \phi_1 + d_f F_d = 0 \tag{2.18}$$

$$d_{21}\frac{d^2\theta}{dt^2} + d_{22}\frac{d^2 x}{dt^2} + h_2 = e_v \tag{2.19}$$

$$d_f = L_{com} - L_{pend} \tag{2.20}$$

$$d_{21} = \frac{R_a L_{\text{com}} \cos(\theta) m_p R_p}{k_1 k_2 N_1} \tag{2.21}$$

$$d_{22} = \frac{R_a R_p \left(N_2 m_{\text{belt}} R_p + m_c + \frac{N_2 J_{\text{motor}}}{R_p} + \frac{2 N_2 J_{\text{pulley}}}{R_p} + m_p \right)}{k_1 k_2 N_1} \tag{2.22}$$

$$h_2 = \frac{R_a R_p \frac{dx}{dt} \left(\frac{k_2 k_3 N_2 N_1^2}{R_a R_p} + \frac{N_2 d_b}{R_p} \right)}{k_1 k_2 N_1} - \frac{R_a L_{\text{com}} \sin(\theta) m_p R_p \left(\frac{d\theta}{dt} \right)^2}{k_1 k_2 N_1} \tag{2.23}$$

$$d_{11} = J_{pend} + L_{\text{com}}^2 m_p \tag{2.24}$$

9

$$d_{12} = L_{\text{com}} \cos(\theta) m_p \tag{2.25}$$

$$h_1 = d_p \frac{d\theta}{dt} \tag{2.26}$$

$$\phi_1 = g L_{\text{com}} \sin(\theta) m_p \tag{2.27}$$

The system model uses parameters measured from the hardware system implemented in the Land Air and Space Robotics (LASR) Lab at Texas A&M University [8,25]. Substituting constants derived for our model we find the final full system dynamics as shown in equations 2.28 and 2.29.

$$\frac{-0.173246 F_d + \cos(\theta)\left(3.2823 e_v + \sin(\theta)\left(\frac{d\theta}{dt}\right)^2 - 156.483 \frac{dx}{dt}\right)}{\cos^2(\theta) - 2.63529} + \frac{8.61577 \sin(\theta) + 0.0103131 \frac{d\theta}{dt}}{\cos^2(\theta) - 2.63529} = \frac{d^2\theta}{dt^2} \tag{2.28}$$

$$\frac{602.471 F_d \cos(\theta) - 30080.1 e_v - 29961.7 \sin(\theta)\cos(\theta)}{3054.2 \cos^2(\theta) - 8048.69} + \frac{-9164.33 \sin(\theta)\left(\frac{d\theta}{dt}\right)^2 - 35.8644 \cos(\theta)\frac{d\theta}{dt} + 1.43406 \times 10^6 \frac{dx}{dt}}{3054.2 \cos^2(\theta) - 8048.69} = \frac{d^2x}{dt^2} \tag{2.29}$$

Equilibrium points of the system are shown in Equation 2.30.

$$x = r \epsilon \mathbb{R}$$
$$\theta = k\pi$$
$$\frac{dx}{dt} = 0 \tag{2.30}$$
$$\frac{d\theta}{dt} = 0$$

II.D.   Linearization

Using equations 2.28 and 2.29 we linearize about the equilibrium at the origin. The linearized system is shown in equation 2.31. The system is controllable, with eigenvalues listed in equation 2.32. Because of the eigenvalue at the origin, we are not able to make claims about the stability of the full nonlinear system by linear analysis [26].

$$
\begin{bmatrix} \dot{\theta} \\ \ddot{\theta} \\ \dot{x} \\ \ddot{x} \end{bmatrix} = \begin{bmatrix} 0 & 1 & 0 & 0 \\ -5.26866 & -0.00630662 & 0 & 95.6912 \\ 0 & 0 & 0 & 1 \\ 5.99895 & 0.00718079 & 0 & -287.128 \end{bmatrix} \begin{bmatrix} \theta \\ \dot{\theta} \\ x \\ \dot{x} \end{bmatrix}
$$
$$
+ \begin{bmatrix} 0 \\ -2.00717 \\ 0 \\ 6.02264 \end{bmatrix} e_v + \begin{bmatrix} 0 \\ 0.105942 \\ 0 \\ -0.120627 \end{bmatrix} F_d
\tag{2.31}
$$

$$
\lambda_1 = -5.438 * 10^{-3} + 1.808j
$$
$$
\lambda_2 = -5.438 * 10^{-3} + 1.808j
$$
$$
\lambda_3 = 0
\tag{2.32}
$$
$$
\lambda_4 = -2.871 * 10^{2}
$$

11

CHAPTER III

TRAJECTORY CONTROL

In this chapter we develop controllers to track pendulum reference trajectories. In this mode of operation, the desired dynamics are predetermined and the testbed is not used to learn about new motions. The prescribed motions can be used to test actuators, sensors, and algorithms. Reference trajectories may be either theoretically constructed or based on data captured from real scenarios. As seen in this chapter, the system structure (e.g. underactuated, nonlinear) makes it very difficult to achieve full trajectory tracking of reference pendulum trajectories. We have however been able to generate approximate tracking of desired trajectories using two separate control schemes.

III.A. Linear Quadratic Integral Control

Using the linearized system as described by equation 2.31 we can derive an optimal linear control. Linear quadratic regulator type control generates proportional gains. Because we expect to track nonzero reference trajectories, to achieve zero steady state error in tracking integral control is needed. Hence an appropriate formulation is that of linear quadratic integral (LQI) control.

We follow the derivation as presented in [27]. Given a standard linear system as shown in equation 3.1 we can optimize the performance index shown in 3.2. Q_y and R are symmetric positive definite, r is a reference trajectory, $v = \dot{u}$. Compared with a standard quadratic cost function we do not penalize control effort, yet instead

penalize changes in the control effort.

$$\dot{x} = Ax(t) + Bu(t)$$

$$y(t) = Cx(t)$$

(3.1)

$$J = \int_0^\infty [y(t) - r]^T Q_y [y(t) - r] + v^T(t) Rv(t) dt$$

(3.2)

Defining the error vector shown in equation 3.3 we can create the new state vector shown in equation 3.4. The new error dynamics are written in equation 3.5.

$$e = y - r$$

(3.3)

$$\tilde{x} = [e^T, (\frac{dx}{dt})^T]^T$$

(3.4)

$$\frac{d\tilde{x}(t)}{dt} = \begin{bmatrix} 0 & C \\ 0 & A \end{bmatrix} \tilde{x}(t) + \begin{bmatrix} 0 \\ B \end{bmatrix} v(t)$$

$$= \tilde{A}\tilde{x}(t) + \tilde{B}v(t)$$

(3.5)

Using the new state the performance index is rewritten as shown in equation 3.6. This performance index matches the form of a standard linear quadratic optimization performance index. Hence we can use the same solution methods for this formulation as is used in the linear quadratic problem.

$$J = \int_0^\infty \tilde{x}^T(t) \begin{bmatrix} Q_y & 0 \\ 0 & 0 \end{bmatrix} \tilde{x}(t) + v^T(t) Rv(t) dt$$

(3.6)

As described in [27], the requirements for the Ricatti equation to have a stationary positive definite solution are the three conditions listed below.

1. Plant is controllable and observable

2. A is nonsingular

3. $CA^{-1}B$ is nonsingular

Because the A matrix in our system is rank-deficient, the necessary conditions are not satisfied. While the position state is needed to fully describe the system, for the control development its removal will allow us to rewrite the system so the necessary conditions are satisfied. Removal of this state will make it so that we cannot track a reference position trajectory of the pendulum. However we can still track the velocity of the body, a reference shown in equation 3.7.

$$v_{ref} = \dot{x} + L_{pend} \cos\theta\dot{\theta} \tag{3.7}$$

After omitting x, the new system is shown in equation 3.8. Each of the necessary conditions is satisfied. By using the small angle approximation on equation 3.7, the linear reference shown in equation 3.9 can be generated. We now are able to solve the optimization using standard linear quadratic solution methods.

$$\begin{bmatrix} \dot{\theta} \\ \ddot{\theta} \\ \ddot{x} \end{bmatrix} = \begin{bmatrix} 0 & 1 & 0 \\ -5.26866 & -0.00630662 & 95.6912 \\ 5.99895 & 0.00718079 & -287.128 \end{bmatrix} \begin{bmatrix} \theta \\ \dot{\theta} \\ \dot{x} \end{bmatrix} + \begin{bmatrix} 0 \\ -2.00717 \\ 6.02264 \end{bmatrix} e_v \tag{3.8}$$

$$y = \begin{bmatrix} 0 & L_{pend} & 1 \end{bmatrix} \begin{bmatrix} \theta \\ \dot{\theta} \\ \dot{x} \end{bmatrix} = C\hat{x} \tag{3.9}$$

The solution to the optimization is of the form shown in equation 3.10. We solve the optimization using $Q_y = 10^5$ and find gains shown in equation 3.11.

$$\begin{aligned} e_v(t) &= K_e \int_0^t [r - y(t)]^T d\tau - K_x \hat{x}(t) \\ &= K_e(x_{ref} - x - L_{pend}\theta) - K_x \hat{x}(t) \end{aligned} \tag{3.10}$$

$$K_{lqi} = \begin{bmatrix} K_e & K_x \end{bmatrix} = \begin{bmatrix} 316.2278 & -839.0478 & 567.7563 & 190.0687 \end{bmatrix} \tag{3.11}$$

III.B. Partial Feedback Linearization

The controller derived in section III.A is limited in that it only drives velocity error to zero. Additionally the integral term slows controller response. For these reasons, in this section we develop an improved trajectory tracking controller using nonlinear control. By examining the dynamics shown in equations 2.18, 2.19 we see that the system is underactuated. In our $n = 2$ degree of freedom system, there are $m = 1$ actuated degrees of freedom and $l = 1$ unactuated degrees of freedom. Our goal is to track a reference trajectory for the pendulum position.

Partial feedback linearization techniques have long been useful to linearize actuated states in a dynamical system [24]. As outlined by Tedrake in [28] we can also attempt to linearize an output which is a function of active and passive joints.

However, referring to equation 2.2 we see that the position is a function of two generalized states. With only one control we are unable to linearize a trajectory which is a function of more generalized states than available controls [29].

Instead, we can linearize the actuated state x and command the trajectory to that state. This neglects the dynamics of the unactuated state θ. To help mitigate undesirable internal dynamics, as developed in [16,17] we can add uncollocated terms to our desired linear dynamics.

To develop the linearizing control, we follow the derivation as presented by Spong in [24]. Beginning from the standard underactuated form presented in Chapter II, with the disturbance force set to zero we solve equation 2.18 for $\ddot{\theta}$. The result of this is shown in equation 3.12. Substituting equation 3.12 into equation 2.19 results in equation 3.13, the terms of which are defined in equation 3.14.

$$\ddot{\theta} = -d_{11}^{-1}(d_{12}\ddot{x} + h_1 + \phi_1) \tag{3.12}$$

$$\bar{d}_{22}\ddot{x} + \bar{h}_2 + \bar{\phi}_2 = e_v \tag{3.13}$$

$$\bar{d}_{22} = d_{22} - d_{21}d_{11}^{-1}d_{12}$$
$$\bar{h}_2 = h_2 - d_{21}d_{11}^{-1}h_1 \tag{3.14}$$
$$\bar{\phi}_2 = -d_{21}d_{11}^{-1}\phi_1$$

$\bar{d}_{22}$ is symmetric positive definite by construction [24]. By choosing the control shown in equation 3.15, the resulting system dynamics are shown in equations 3.16, 3.17. x is linearized, with θ dynamics remaining nonlinear.

$$e_v = \bar{d}_{22}\nu_2 + \bar{h}_2 + \bar{\phi}_2 \tag{3.15}$$

$$d_{11}\ddot{\theta} + h_1 + \phi_1 = -d_{12}\nu_2 \tag{3.16}$$

$$\ddot{x} = \nu_2 \tag{3.17}$$

To track a reference trajectory, we choose ν_2 as shown in equation 3.18. By introducing new states as shown in equation 3.19, the full system dynamics can be rewritten. These dynamics are shown in equations 3.20, 3.21, 3.22, 3.23.

$$\nu_2 = \ddot{x}_{ref} + k_d(\dot{x}_{ref} - \dot{x}) + k_p(x_{ref} - x) \tag{3.18}$$

$$
\begin{aligned}
z_1 &= x - x_{ref} \\
z_2 &= \dot{x} - \dot{x}_{ref} \\
\eta_1 &= \theta \\
\eta_2 &= \dot{\theta}
\end{aligned}
\tag{3.19}
$$

$$\dot{z}_1 = z_2 \tag{3.20}$$

$$\dot{z}_2 = -k_p z_1 - k_d z_2 \tag{3.21}$$

$$\dot{\eta}_1 = \eta_2 \tag{3.22}$$

17

$$\dot{\eta}_2 = -d_{11}^{-1}(h_1 + \phi_1) - d_{11}^{-1}d_{12}(\ddot{x}_{ref} - k_p z_1 - k_d z_2) \tag{3.23}$$

Setting z to zero, the zero dynamics of the system can be analyzed. As done in [17], a $\dot{\theta}$ term can be added to ν_2 for damping to the internal dynamics. With this included, the expression for ν_2 is shown in equation 3.24. The total control for our system model parameters is shown in equation 3.25.

$$\nu_2 = \ddot{x}_{ref} + k_d(\dot{x}_{ref} - \dot{x}) + k_p(x_{ref} - x) - k_\theta \dot{\theta} \tag{3.24}$$

$$e_v = \nu_2 \left(0.267576 - 0.101536 \cos^2 \theta\right) - 0.996065 \sin \theta \cos \theta \\ - 0.304665 \sin \theta \dot{\theta}^2 - 0.0011923 \cos(\theta)\dot{\theta} + 47.6747\dot{x} \tag{3.25}$$

To analyze system stability, we use the approach presented in [16]. First we find the internal dynamics and linearize about the origin. We insert the ν_2 expression from equation 3.24 into equation 3.16. Expanding all terms and setting x and x_{ref} and their derivatives to zero results in the zero dynamics shown in 3.26.

$$\frac{\dot{\theta}\left(L_{\mathrm{com}}\cos(\theta)k_\theta m_p - d_p\right)}{J_c + L_{\mathrm{com}}^2 m_p} - \frac{gL_{\mathrm{com}}\sin(\theta)m_p}{J_c + L_{\mathrm{com}}^2 m_p} = \ddot{\theta} \tag{3.26}$$

Linearizing the zero dynamics about the equilibrium point of the origin, we find the resulting linear system shown in equation 3.27.

$$\begin{bmatrix} \dot{\theta} \\ \ddot{\theta} \end{bmatrix} = \begin{bmatrix} 0 & 1 \\ -\frac{gL_{\mathrm{com}}m_p}{J_c + L_{\mathrm{com}}^2 m_p} & \frac{k_\theta L_{\mathrm{com}}m_p - d_p}{J_c + L_{\mathrm{com}}^2 m_p} \end{bmatrix} \begin{bmatrix} \theta \\ \dot{\theta} \end{bmatrix} \\ = \begin{bmatrix} 0 & 1 \\ A_{21} & A_{22} \end{bmatrix} \begin{bmatrix} \theta \\ \dot{\theta} \end{bmatrix} \tag{3.27}$$

The eigenvalues of the system can be found as shown in equation 3.28. There are two scenarios in which the system is hurwitz. The first case is with two negative real eigenvalues, and the second case is with two complex eigenvalues with negative real parts. The requirement on k_θ for the system to have two complex stable eigenvalues is shown in equation 3.29. Conditions 3.30, 3.31 must be satisfied for the system to have two stable real eigenvalues.

$$\lambda_{1,2} = -\frac{A_{22}}{2} \pm \frac{(A_{22}^2 + 4A_{21})^{\frac{1}{2}}}{2} \tag{3.28}$$

$$\frac{d_p m_p}{L_{\text{com}}} < k_\theta < \frac{(J_c + L_{\text{com}}^2 m_p)\left(\frac{2L_{\text{com}}d_p m_p}{J_c + L_{\text{com}}^2 m_p} + \frac{4\sqrt{g}L_{\text{com}}^{3/2}m_p^{3/2}}{\sqrt{J_c + L_{\text{com}}^2 m_p}}\right)}{2L_{\text{com}}^2 m_p^2} \tag{3.29}$$

$$k_\theta > \frac{(J_c + L_{\text{com}}^2 m_p)\left(\frac{2L_{\text{com}}d_p m_p}{J_c + L_{\text{com}}^2 m_p} + \frac{4\sqrt{g}L_{\text{com}}^{3/2}m_p^{3/2}}{\sqrt{J_c + L_{\text{com}}^2 m_p}}\right)}{2L_{\text{com}}^2 m_p^2} \tag{3.30}$$

$$\frac{d_p - k_\theta L_{\text{com}} m_p}{2J_c + 2L_{\text{com}}^2 m_p} < -0.5 \left(\frac{(d_p - k_\theta L_{\text{com}} m_p)^2 - 4gL_{\text{com}}m_p(J_c + L_{\text{com}}^2 m_p)}{(J_c + L_{\text{com}}^2 m_p)^2}\right)^{0.5} \tag{3.31}$$

In either of the two cases the zero dynamics are strictly stable, hence by Lyapunov's linearization method [26] the origin is asymptotically stable (in the full nonlinear system). Because the zero dynamics are asymptotically stable at the origin, we say that the system is minimum phase.

CHAPTER IV

ANGLE REGULATION CONTROL

In this chapter we discuss a method to simulate contact dynamics interactions without prescribing motion through predetermined trajectories. The controller creates conditions necessary for the body dynamics to be affected only by contact forces and torques. This chapter develops the methodology used for this type of simulation and presents a nonlinear controller which creates the desired system response.

IV.A. Methodology

Using equation 2.10 we can inspect the effect of the contact force on the system. As shown in equation 4.1, we regard θ as a small constant ϵ. Applying the small angle approximation to 2.10, the resulting dynamics are shown in equation **??**

$$\theta = \epsilon_0 + \epsilon \rightarrow \theta = \epsilon \tag{4.1}$$

$$\frac{gL_{com}\epsilon m_p + L_{com}m_p\ddot{x}}{L_{pend} - L_{com}} = F_d \tag{4.2}$$

This development shows that for small angles, the x dynamics are only a function of the contact force. If the angle in the pendulum is regulated and the pendulum dynamics effectively removed, the body will remain in the plane with a planar acceleration being proportional to the input contact forces. This enables a realistic simulation of unknown contact dynamics to occur as expected from Newtonian physics. By regulating the angular dynamics, we can simulate unknown contact dynamics.

As shown in equation 4.3, by setting $\ddot{x} = 0$ we see there is a residual term from the pendulum dynamics. These dynamics create a deadband in which force inputs do not result in body motion. Robot interactions should be planned with knowledge of this deadband, and consequently any accelerations in the body must be interpreted using this relation.

$$
\begin{aligned}
F_{dmin} &= \frac{gL_{com}\epsilon m_p + L_{com}m_p\ddot{x}}{L_{pend} - L_{com}}\Big|_{\ddot{x}=0} \\
&= \frac{gL_{com}\epsilon m_p}{L_{pend} - L_{com}}
\end{aligned}
\tag{4.3}
$$

In our simulations, a bias term is added to all forces delivered to the pendulum so as to avoid the deadband region. The magnitude of the small angle used in our simulation corresponds to a single encoder count. As shown in equation 4.4, the sign of epsilon should match the direction in which force is applied. These details are handled externally by the planning engine running the robot delivering the contact forces.

$$
\epsilon = sgn(F_d)\epsilon_{mag}, \epsilon_{mag} > 0
\tag{4.4}
$$

IV.B.   Uncollocated Partial Feedback Linearization

To control and regulate the angular dynamics we use an extension of the previously presented partial feedback linearization [24]. The angular states are unactuated and not directly controlled. Spong shows that if certain coupling conditions are satisfied, the unactuated states can be successfully linearized. This uncollocated partial feedback linearization uses integral backstepping to construct a linearizing control

for the unactuated states.

We start from the system shown in equations 3.16, 3.17. The condition shown in equation 4.5 is necessary for what Spong calls strong inertial coupling. This inertial coupling is explained as an analog of controllability for use of the backstepping method. Examining equation 2.25 we see this strong intertial coupling requirement for our system is satisfied within our operating range in which $\theta \ll \frac{\pi}{2}$.

$$rank(d_{12}(\theta, x)) = l = 1, \forall(\theta, x) \tag{4.5}$$

Because the strong inertial coupling requirement is satisfied and d_{12} is scalar, we can compute the pseudoinverse of d_{12} as in equation 4.6. Using this inverse, ν_2 is found as shown in equation 4.7.

$$d_{12}^\dagger = d_{12}^T(d_{12}d_{12}^T)^{-1} = d_{12}^{-1} \tag{4.6}$$

$$\nu_2 = -d_{12}^{-1}(d_{11}\nu_1 + h_1 + \phi_1) \tag{4.7}$$

With this choice of ν_2 the resulting system is as shown in equations 4.8, 4.9. The corresponding input is shown in equation 4.10, with coefficients defined in equation 4.11.

$$\ddot{\theta} = \nu_1 \tag{4.8}$$

$$d_{12}\ddot{x} + h_1 + \phi_1 = -d_{11}\nu_1 \tag{4.9}$$

$$e_v = \bar{d}_{21}\nu_1 + \bar{h}_2 + \bar{\phi}_2 \tag{4.10}$$

$$\bar{d}_{22} = d_{21} - d_{22}d_{12}^{-1}d_{11}$$

$$\bar{h}_2 = h_2 - d_{22}d_{12}^{-1}h_1 \tag{4.11}$$

$$\bar{\phi}_2 = -d_{22}d_{12}^{-1}\phi_1$$

Because in this case we are only regulating the angular state, linearization alone is adequate and the control does not need to be formulated as a tracking problem. The control input for our system is shown in equation 4.12 with ν_1 chosen as shown in equation 4.13.

$$\begin{aligned} e_v = {} & 0.304665\nu_1 \cos\theta - 0.802879\nu_1 \sec\theta - 2.62492\tan\theta \\ & - 0.304665\sin\theta\dot{\theta}^2 - 0.00314205\sec\theta\dot{\theta} + 47.6747\dot{x} \end{aligned} \tag{4.12}$$

$$\nu_1 = -k_d\dot{\theta} - k_p\theta \tag{4.13}$$

CHAPTER V

SIMULATION

In this chapter the simulation structure is described and the controllers developed in chapters III and IV are tested.

V.A.   Simulation Structure

The simulations are based on the three contact force cases shown in Figure V.1. The goal body trajectories for each of these test cases are derived using equation 4.2. Using this relation, the bias term is subtracted from the input force to determine the expected goal x dynamics. These reference dynamics are shown in figure V.2.
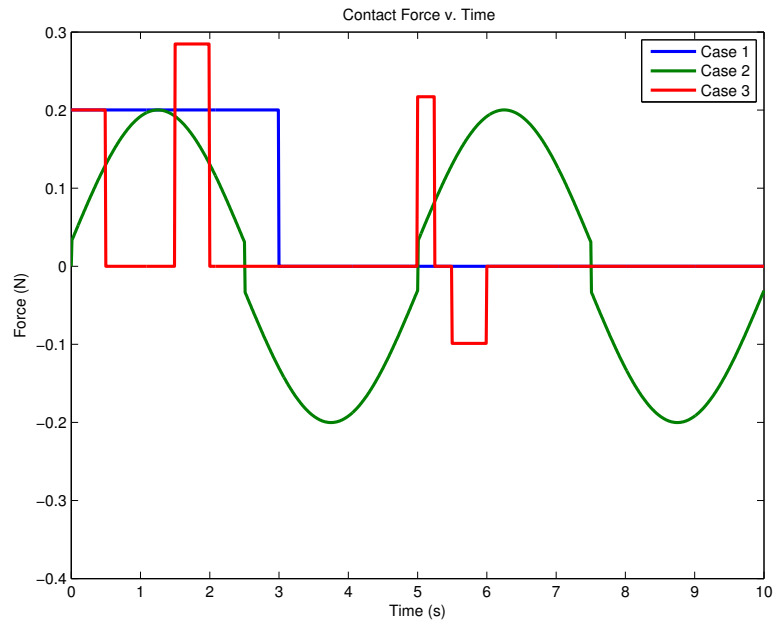

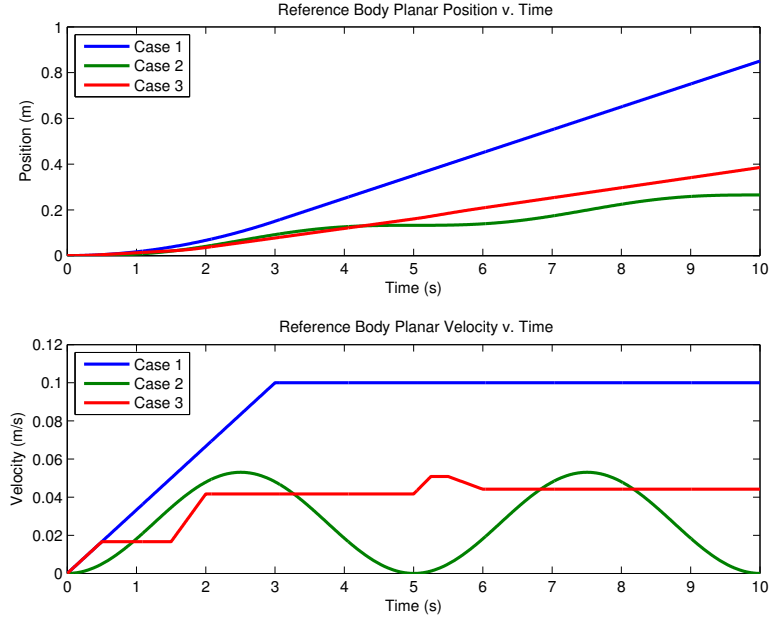**Figure V.1. Contact force time history for each test case**

Figure V.2. Reference dynamics for each test case

The simulation consists of three main substructures: dynamics, measurements, controller. Each of these areas has been implemented as separate a function in Matlab. The full nonlinear dynamics are propagated at a rate equal to the fastest measurements (100 Hz). The truth dynamics are input to a measurement model to simulate noisy sensor readings.

Angular measurement is simulated as being recorded from a 10,000 count encoder to which is discretization error is added. To smooth the data, the measurements are inserted into an α filter, the model of which is shown in equation 5.1. The angular rate is simulated as measured from a gyroscope with appropriate white noise added. The noisy measurement is passed through a first order low pass filter filter.

$$\hat{\theta}_k = \hat{\theta}_{k-1} + h\hat{\dot{\theta}}_{k-1}$$

$$r = \tilde{\theta} - \hat{\theta}_k \tag{5.1}$$

$$\hat{\theta}_k = \hat{\theta}_k + \alpha r$$

While the angular rate and angle are measured at 100 Hz, the position measurements are recorded at 50 Hz from encoders on board the motor. These encoders are at a much lower resolution with only 2000 counts per revolution. The position measurements are taken directly from encoder reading without smoothing or filtering. The velocity is not measured directly but is estimated by the finite difference method on the position measurements. A first order low pass filter is applied to the output to reduce the frequency content [30].

V.B.   Trajectory Control Results

The trajectory tracking errors of all three force cases are shown in figures V.3, V.4. The peak errors are shown in table V.1. Examining the LQI performance, we note from the position plot that in test cases 1 and 3 there is a large steady state error which does not appear to be converging to zero. This behavior is not surprising as we removed the position state from the tracking formulation and instead are only tracking velocity.

Looking to figure V.4 as expected we see that the LQI velocity errors converge to zero for test cases 1 and 3. However for test case 2 the errors do not converge to zero. This is the only test case which is sinusoidal and the reference does not stabilize to a fixed value over time. It appears there is a phase offset due to the delay
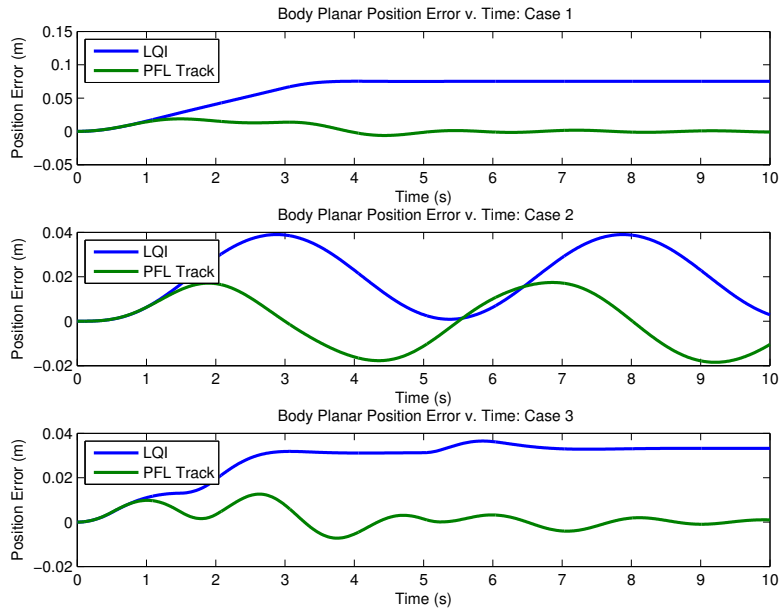
26

Figure V.3. Position trajectory tracking error for each test case

introduced by the integrator.

The LQI velocity errors converge rapidly to zero in test cases 1 and 3 after the reference stabilizes, yet error increases when the setpoint changes. This response in velocity can be further tuned by adjusting the weighting matrix in optimization. Based on the velocity results, the controller appears to be performing as designed.

Examining figure V.3 and focusing now on the PFL performance, we see that there is converging position error in test cases 1 and 3. The initial behavior is subject to some disturbance, but this is expected as we are not regulating angular states directly. Performance in test case 2 is very similar in error to the LQI controller.

The velocity results in figure V.4 show converging velocity error for cases 1 and 3. However, in comparing to the zero steady state velocity error with the LQI controller, the PFL controller has noticeable perturbations from zero error.

controller	max position error (m)	max velocity error (m/s)
LQI Case 1	0.0753	0.0262
PFL Case 1	0.0188	0.0238
LQI Case 2	0.0390	0.0244
PFL Case 2	0.0185	0.0248
LQI Case 3	0.0365	0.0239
PFL Case 3	0.0126	0.0283

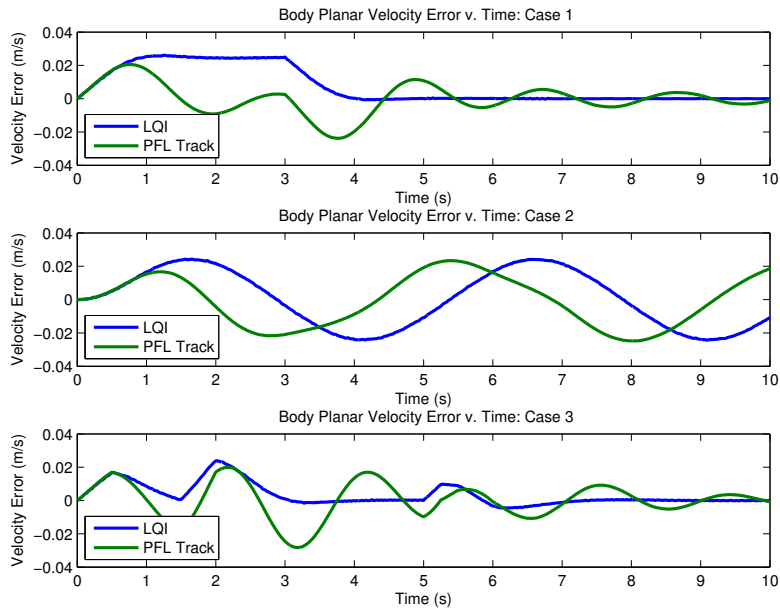**Table V.1. Peak trajectory tracking controller errors**

Figure V.4. Velocity trajectory tracking error for each test case

The PFL response can be explained by recalling equation 3.24 and inspecting figure V.5. The only angular regulation is in the form of the damping term $\dot{\theta}$ in ν_2. As seen in figure V.5, for each test case, especially in case 3, there is a large
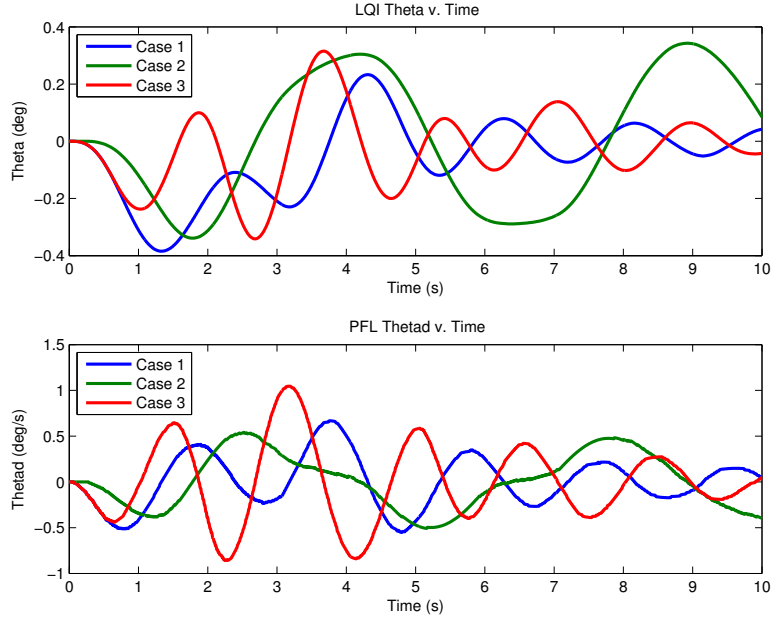
Figure V.5. θ **response for PFL controller**

jump in angular rate. These perturbations in angular dynamics are the source of the oscillations in trajectory error for the PFL controller. We see the trajectory error disturbances do eventually stabilize. This controlled stabilization through feedback is preferred to relying on the natural system damping to remove angular oscillations.

The control efforts of each controller are shown in figure V.6. The oscillations introduced by $\dot{\theta}$ are visible in the PFL based control. Both control outputs are bounded and within the range of acceptable motor inputs.

V.C. Angle Regulation Control Results

The results of simulating the PFL angle regulation controller are shown in figures V.7, V.8. The peak errors are shown in table V.2. The errors are smallest in case 2 where there is a large sustained contact. The errors are largest when there are
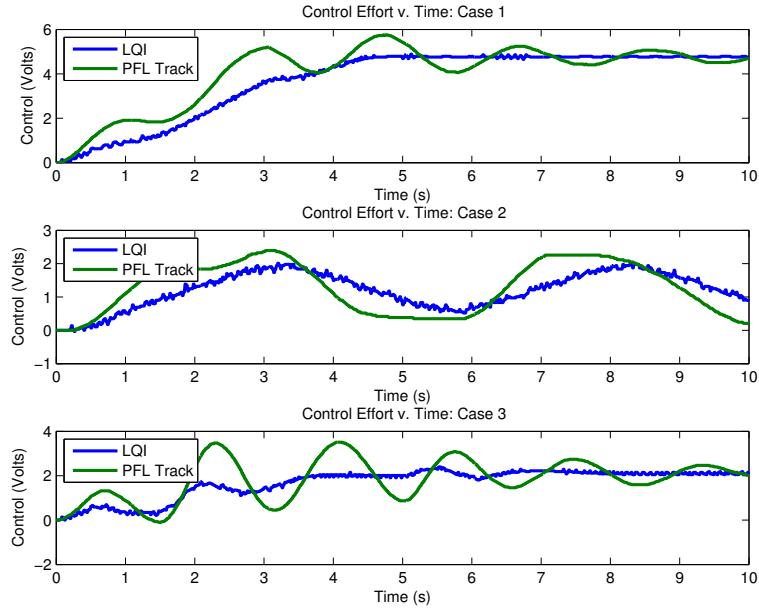
Figure V.6. Control effort for trajectory controllers

multiple perturbations as in case 3.

Comparing the results to the tracking controller results in the previous chapter, the velocity errors in this new controller are significantly lower. In cases 1 and 2 the errors are one order of magnitude reduced. However, the position errors are larger in all cases but case 2. The position errors are especially large in case 3 where multiple impacts are simulated.

test case	max position error (m)	max velocity error (m/s)
1	0.0220	0.0041
2	0.0046	0.0053
3	0.0411	0.0106

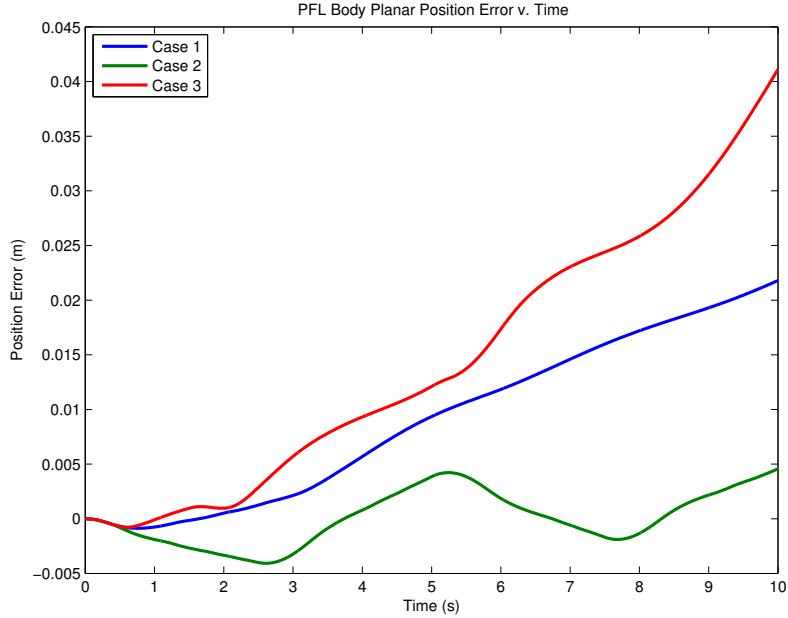**Table V.2. Peak angle regulator controller errors**

Figure V.7. Position trajectory error for angle regulation controller

In this control scheme there is no specification of desired behavior. When there is a force, regulating the angular dynamics is sufficient to create resultant motion in the body as approximated by equation 4.2. Once the contact forces are removed, the controller only continues to regulate the angular dynamics. Over time, any small velocity errors when compared to the goal velocity will not be zeroed, but will remain constant in the absence of further perturbations. As shown in figure V.8 the velocity errors in cases 1 and 3 are not centered around zero, but are nonzero and near constant in the absence of further perturbation. Over time the tiny errors in velocity compound to growing error in position.

In case 2 the body is always subject to a contact force imparting an acceleration and there is no accumulation of position error. During contact the velocity error oscillates around zero, thereby ensuring against buildup of position error. Examining
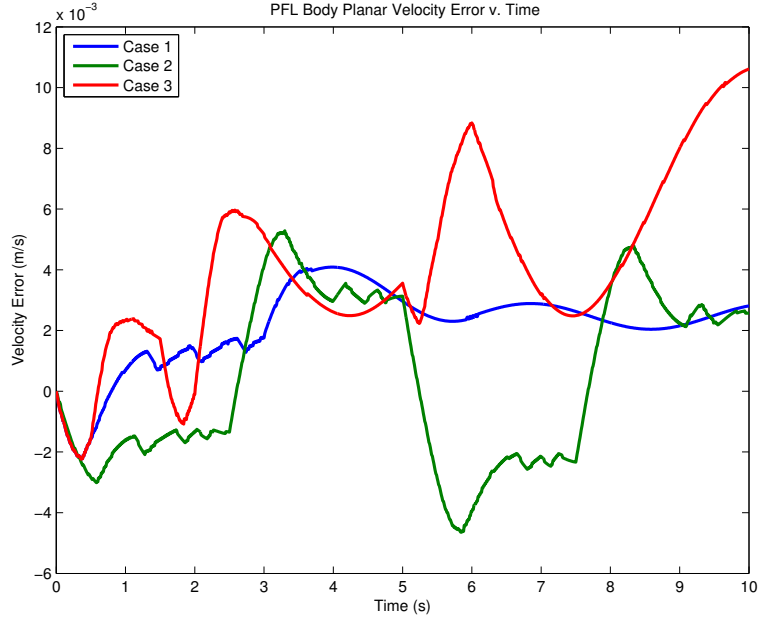
31

Figure V.8. Velocity trajectory error for angle regulation controller

the early period of case 1 while contact is occurring, we see similar behavior in that the error is very small in the neighborhood of the interaction. From this we conclude that the angle regulation controller is very successful in simulating contact dynamics during interactions and in the neighborhood after interactions. Post interaction, position error compounds over time due to the presence of small velocity error.

Figure V.9 shows the angular states for the PFL regulation controller in all the test cases. The angles are regulated to one encoder tick, and the rates are quickly regulated as well. The control effort is shown in figure V.10. The voltage command is within specification and there is no jitter or undesired oscillation.
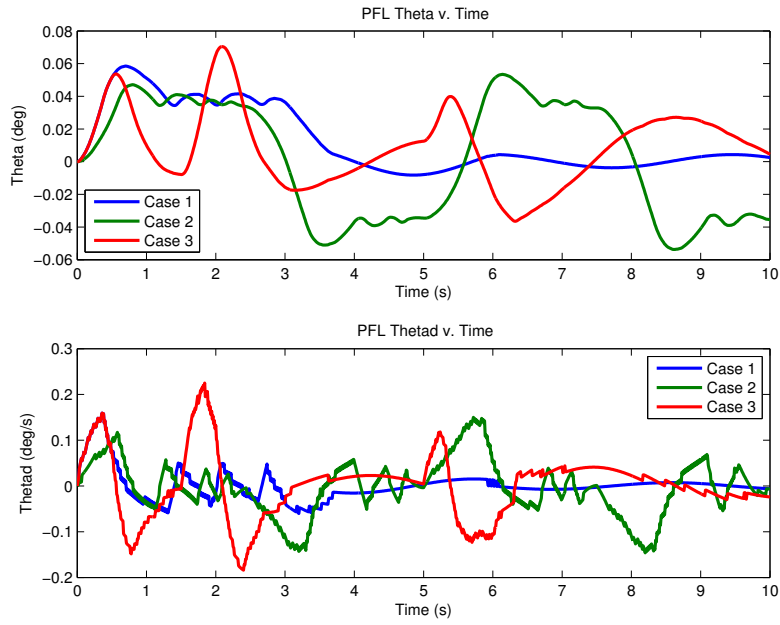
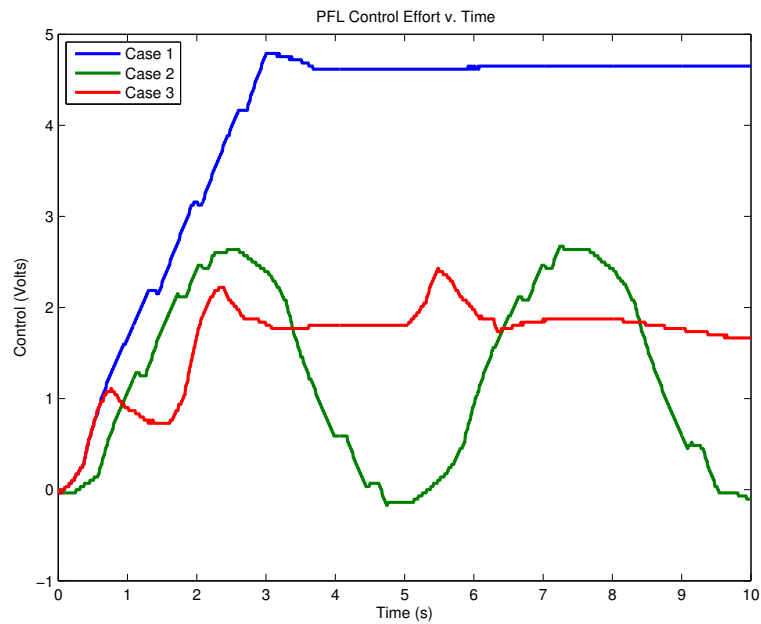Figure V.9. Angular states for angle regulation controller

Figure V.10. Control effort for angle regulation controller

CHAPTER VI

CONSIDERATIONS FOR HARDWARE IMPLEMENTATION

Attempts were made to incorporate the simulated controllers into the upgraded hardware developed in [25]. In this section, we will outline reasons why this effort was unsuccessful and suggest modifications to the hardware which will likely yield better results.

The primary cause of controller failure was due to the unmodeled dynamics present in the system. Although great care was taken into determining the pendulum moment of inertia, and center of mass, the rigid body assumption did not hold in the real hardware. The carbon fiber rod which makes up most of the length of the pendulum is nonrigid and fast acceleration of the cart causes low frequency vibration modes in the rod.

This can be demonstrated in an experiment conducted in the hardware. As shown in figure VI.1 a constant input is applied to the motors for a short time, followed by a sudden zero input to the motors. As shown in figure VI.2, while there is an initial oscillation in angle due to the motion starting from rest, when the control signal goes to zero a high frequency component in introduced in the angular states.

Using the fourier transform we can analyze the frequency content of the angular rate as shown in figure VI.3. The pendulum natural frequency corresponds to the spike at 0.2 Hz, while the remaining frequency content is due to vibration. Finite impulse response lower pass filters were designed for the angular rate measurements, however the delay introduced significantly slowed control response.
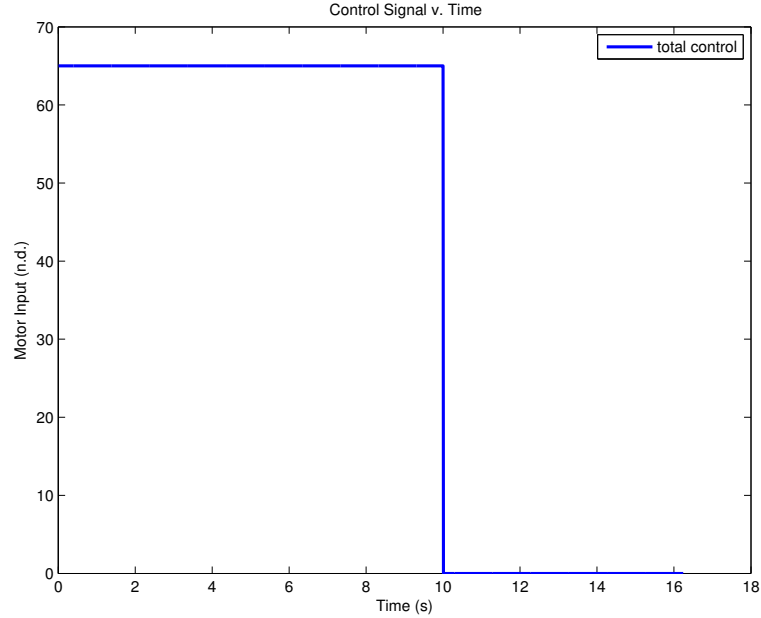
Figure VI.1. Control signal in hardware experiment

Instead of processing the data to fit our expected system response, it makes more sense to either redesign the system to better match the rigid body assumption, or to develop controllers based around a flexible system. In addition to reducing the vibrations in the pendulum, other concerns such as slop in the joints must be addressed. Even if the flexible modes cannot be mitigated through hardware redesign, the hardware in its current state needs improvement.
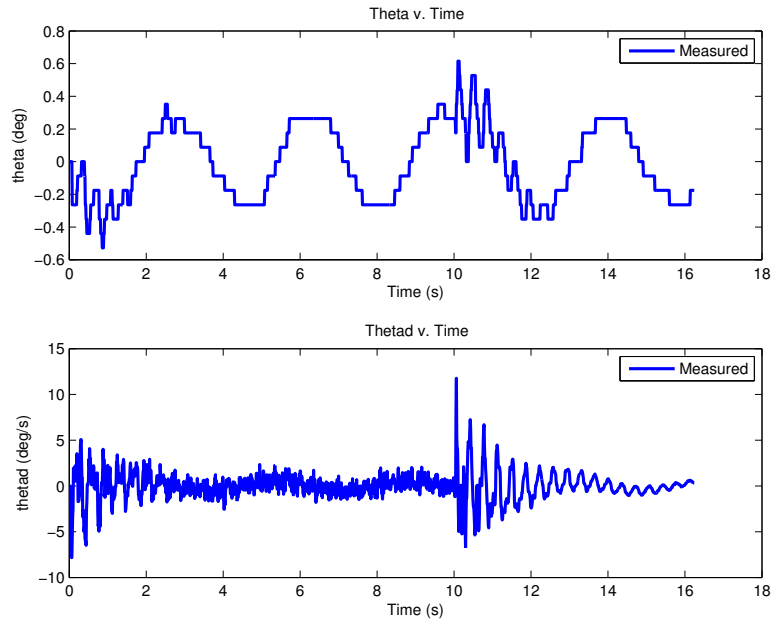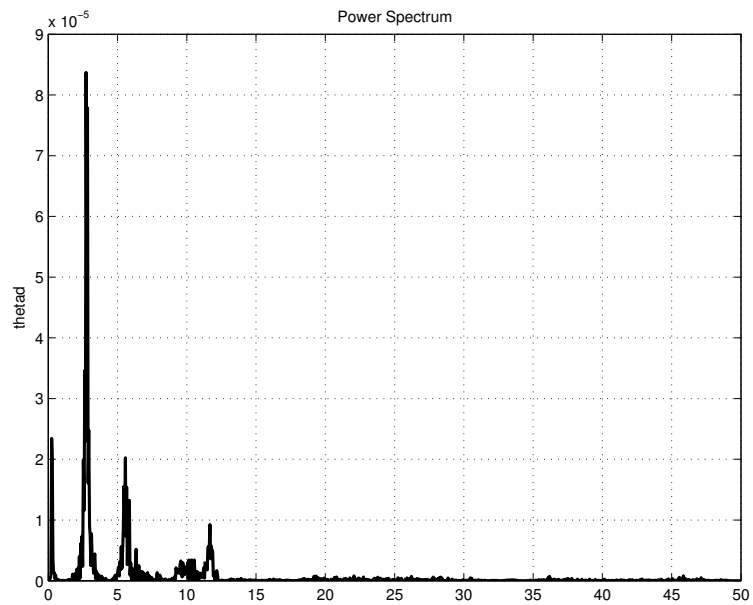
Figure VI.2. Angular states in hardware experiment

Figure VI.3. $\dot{\theta}$ frequency response in hardware experiment

CHAPTER VII

CONCLUSION

Proximity operations and contact dynamics simulations typically prescribe trajectories for vehicle motion. While this is valuable, simulating unknown interactions is important and allows for insights into algorithm and sensor performance that can be neglected by tracking predefined trajectories. This thesis developed controllers for both trajectory tracking simulations and for simulations of unknown contact dynamics.

The work done in this thesis shows that the angle regulation controller is a very good method to simulate unknown contact interactions. Performance during and in the neighborhood of interactions outperforms trajectory tracking. The performance of the trajectory tracking controllers was acceptable. The nonlinear trajectory tracking controller outperformed the linear controller when comparing peak errors. Tracking using a fully actuated robot or robots could likely produce better results than the trajectory tracking controllers presented here.

The failure of the controllers in hardware opens up several directions for future work. If the hardware can be designed and implemented to better match the rigid body assumptions in this thesis, then the controls developed here would likely perform better in hardware. The other approach would would be to explore controllers based around a flexible body model. The work done by Olfati-Saber in the control of underactuated flexible end effectors would be a good starting point for such efforts [31]. Regardless of the redesign, the gantry crane system has been shown to be

a useful tool for both prescribed and unknown contact dynamics simulations.

REFERENCES

[1] University of Michigan, "DC Motor Speed: System Modeling," Available online: `http://ctms.engin.umich.edu/CTMS/index.php?example=MotorSpeed&section=SystemModeling`, [Accessed 05-May-2016].

[2] Liou, J. and Johnson, N., "A sensitivity study of the effectiveness of active debris removal in LEO," *Acta Astronautica*, Vol. 64, 2009, pp. 236–243.

[3] Liou, J., Johnson, N., and Hill, N., "Controlling the growth of future LEO debris populations with active debris removal," *Acta Astronautica*, Vol. 66, 2010, pp. 648–653.

[4] Liou, J. C. and Shoots, D., "Monthly Number of Objects in Earth Orbit by Object Type," *The Orbital Debris Quarterly News*, Vol. 30, No. 6, 2014.

[5] Lockheed Martin Corporation, "Space Operations Simulation Center," Available online: `http://www.lockheedmartin.com/us/ssc/sosc.html`, [Accessed 29-Jan-2016].

[6] J. DiMatteo, D. Florakis, A. W. and Milam, M., "Proximity Operations Testing with a Rotating and Translating Resident Space Object," *AIAA Guidance, Navigation, and Control Conference*, Chicago, IL, August 2009.

[7] Jet Propulsion Laboratory, "Formation Control Testbed," Available online: `http://dst.jpl.nasa.gov/test_beds`, [Accessed 28-Jan-2016].

[8] Probe, A., *Development of a Robotic Simulation Platform for Spacecraft Proximity Operations and Contact Dynamics Experiments*, Master's thesis, Texas A&M University, 2013.

[9] A. Probe, J. J., "Development of a Robotic Simulation Platform for Spacecraft Proximity Operations and Contact Dynamics Experiments," *AIAA Guidance, Navigation, and Control Conference, AIAA SciTech*, National Harbor, MD, January 2014.

[10] P. Valle, L. Dungan, T. Cunningham, A. Lieberman, D. Poncia, "Active Response Gravity Offload System," Available online: `https://ntrs.nasa.gov/search.jsp?R=20120000452`, [Accessed 12-Oct-2016].

[11] Hockman, B., Frick, A., Nesnas, I. A., and Pavone, M., "Design, Control, and Experimentation of Internally-Actuated Rovers for the Exploration of Low-Gravity Planetary Bodies," *Field and Service Robotics*, Springer, 2015, pp. 283 – 298.

[12] Kumar, E. V. and Jerome, J., "Robust LQR controller design for stabilizing and trajectory tracking of inverted pendulum," *Procedia Engineering*, Vol. 64, 2013, pp. 169 – 178.

[13] Omar, H. M., *Control of Gantry and Tower Cranes*, Ph.D. thesis, Virginia Polytechnic Institute and State University, 2003.

[14] Wang, J.-J., "Stabilization and tracking control of XZ inverted pendulum with sliding-mode control," {ISA} *Transactions*, Vol. 51, No. 6, 2012, pp. 763 – 770.

[15] Yu, H., Liu, Y., and Yang, T., "Tracking Control of a Pendulum-driven Cart-pole Underactuated System," *2007 IEEE International Conference on Systems, Man and Cybernetics*, Oct 2007, pp. 2425–2430.

[16] Tuan, L. A., Kim, G. H., and Lee, S. G., "Partial Feedback Linearization Control of the Three Dimensional Overhead Crane," *2012 IEEE International Conference on Automation Science and Engineering (CASE)*, Aug 2012, pp. 1198–1203.

[17] X. Zhang, B. Gao, H. C., "Nonlinear Controller for a Gantry Crane Based on Partial Feedback Linearization," *International Conference on Control and Automation*, Budapest, Hungary, June 2005.

[18] Davis, J., Doebbler, J., Daugherty, K., Junkins, J., and Valasek, J., "Aerospace Vehicle Motion Emulation Using Omni-directional Mobile Platform," *AIAA Guidance, Navigation and Control Conference*, Hilton Head, South Carolina, August 2007.

[19] Doebbler, J., Davis, J., Junkins, J., and Valasek, J., "Mobile Robotic System for Ground Testing of Multi-Spacecraft Proximity Operations," *AIAA Guidance, Navigation and Control Conference*, Honolulu, Hawaii, August 2008.

[20] Peter Dourmashkin, "Chapter 24: Physical Pendulum (Course Notes for MIT 8.01)," Available online: `http://web.mit.edu/8.01t/www/coursedocs/current/guide.htm`, [Accessed 12-Oct-2016].

[21] Ogata, K., *Modern Control Engineering*, Prentice Hall, Upper Saddle River, NJ, 2010.

[22] Parker Hannifin, "Engineering Reference Table: Motor Sizing and Selection Process," Available online: `http://www.parkermotion.com/literature/pg223_engrg.htm`, [Accessed 12-Oct-2016].

[23] Mazurkiewicz, J., "The basics of motion control - Part 1," *Precision Motor Control*, 1995, pp. 43–45.

[24] Spong, M., "The Control of Underactuated Mechanical Systems," *First International Conference on Mechatronics*, Mexico City, Mexico, 1994.

[25] J. J. Davis, "Enabling Large-body Active Debris Removal: Phase II Final Report," Available by request: `http://www.vectornav.com/`, [Accessed 09-Oct-2016].

[26] Slotine, J.-J. and Li, W., *Applied Nonlinear Control*, Prentice Hall, Englewood Cliffs, NJ, 1991.

[27] Masayoshi Tomizuka, "LQI Controller for Continuous Time Systems (Course Notes from UC Berkeley ME232)," Available online: `http://www.egr.msu.edu/classes/me851/jchoi/lecture/LQI-note.pdf`, [Accessed 09-Oct-2016].

[28] Russ Tedrake, "Underactuated Robotics: Algorithms for Walking, Running, Swimming, Flying, and Manipulation (Course Notes for MIT 6.832)," Available online: `http://underactuated.mit.edu/`, [Accessed 09-Oct-2016].

[29] Shkolnik, A. and Tedrake, R., "High-Dimensional Underactuated Motion Planning via Task Space Control," *Proceedings of the IEEE/RSJ International Conference on Intelligent Robots and Systems (IROS)*, IEEE/RSJ, 2008.

[30] D. J. Block, K. J. Astrom, M. W. S., *The Reaction Wheel Pendulum*, Morgan and Claypool, 2007.

[31] Olfati-Saber, R., *Nonlinear Control of Underactuated Mechanical Systems with Application to Robotics and Aerospace Vehicles*, Ph.D. thesis, Massachusetts Institute of Technology, 2000.